Eur. J. Mineral., 34, 259–274, 2022
https://doi.org/10.5194/ejm-34-259-2022

European Journal of Mineralogy
Open Access

The effect of Co substitution on the Raman spectra of pyrite: potential as an assaying tool

Khulan Berkh and Dieter Rammlmair

Federal Institute for Geosciences and Natural Resources, Stilleweg 2, 30655 Hanover, Germany

Correspondence: Khulan Berkh (khulan.berkh@bgr.de)

Received: 2 December 2021 – Revised: 4 March 2022 – Accepted: 21 March 2022 – Published: 14 April 2022

Abstract. The textural appearance of Co-bearing pyrite was visualized by a mapping method using a Raman microprobe. Two out of five Raman active modes (E_g and A_g) of pyrite were evaluated here. The obtained Raman map tightly correlates with a Co distribution map revealed by electron microprobe. Both E_g and A_g modes gradually downshift and broaden with increasing Co concentration. The broadening and shifting of the A_g mode is stronger compared to the E_g mode. Especially the intensity of the A_g mode drastically drops and diminishes in comparison to the E_g mode. Both 532 and 633 nm lasers revealed the same variation in position and width of the E_g and A_g modes. Only the intensity ratio of the modes differed because of an energy-dependent resonance scattering from the A_g mode. The 1064 nm laser was unsuitable since the Raman scattering intensity is inversely proportional to wavelength. Furthermore, highly broadened Raman modes at upshifted frequencies caused by the standard mechanical polishing could be avoided by analyzing cut or polished samples with a broad ion beam.

1 Introduction

Fast appraisal of high value metal distribution within sulfides is important in all the exploration, selective mining, and processing sides of the mineral industry. In Chile, small-scale mining is often related to mineral treatment and melting facilities of ENAMI, a state company providing small-scale miners a selling platform for their products with the main focus on Cu, Mo, Au, and A_g. Since hundreds of small mines deliver their ores to ENAMI, valuable metals such as Co, enriched in one or the other mine site, are diluted by mixing with other sources rather than extracted and consequently deposited in tailings dumps. Thus, assaying ore from different sources prior to crushing and subsequent separation of Co-rich ore before mixing with common pyrites would help to sell the concentrates enriched in Co to prospective buyers. Recovery from tailings, in which both Co-rich and Co-free pyrites are mixed together, would only be possible due to localizing zones of Co-rich pyrites in the sense of selective mining by screening methods.

More importantly, internal textures such as chemical zoning, overgrowth, and brecciation of the mineral of economic interest provide valuable information regarding ore genesis and accordingly spatial distribution of target metals within the deposit. However, such textures based on small chemical heterogeneities, for example resulting from Co, cannot be distinguished by many standard methods or can only be recognized with considerable effort. Thus, we test a Raman technique on Co-bearing pyrite focusing on the most suitable setting for its possibly fast and accurate identification and textural characterization, as well as quantitative estimation of Co concentration.

An old mine tailings dump of Delirio mine located 6 km south of Punitaqui in north-central Chile was geochemically and mineralogically investigated for its economic potential and environmental impact (Berkh et al., 2019). Delirio mine exploited mainly Cu and subsidiary Au ($3\,g\,t^{-1}$) ore during the first half of the 20th century (Sillitoe and Thompson, 1998; Goodwin et al., 2018). Geologically, Delirio mine is situated in the southern part of the Mantos de Punitaqui vein that is some 4.5 km long and 4 m wide, and it extends vertically > 300 m. The vein is hosted by a north-striking and steeply dipping fault in Mesozoic Coastal Batholith, a calc-alkaline, I type, and magnetite-series suite (Fig. 1).

Unfortunately, the mineralogy of the Delirio mine is hardly known. In contrast, the mineralogy of the Los Man-

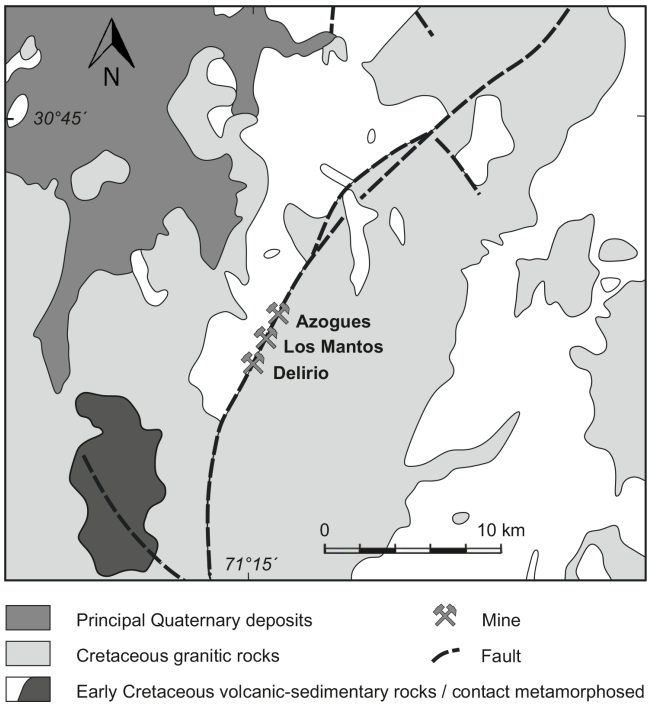

Figure 1. Geological map of the Mantos de Punitaqui district, northern Chile, showing control of the vein by major arc-parallel fault along pluton contact (modified based on Sillitoe and Thompson, 1998).

tos mine, located in the central part of the Mantos de Punitaqui vein (Fig. 1) and representing the Au-rich part of the system, is well studied. The mineralogy consists mainly of quartz, calcite, specular hematite, magnetite, chalcopyrite, and pyrite. The Azogues mine located in the northern part of the vein, in turn, exploited mercury. All three deposits in the Mantos de Punitaqui vein can be considered iron oxide–copper–gold (IOCG) deposits due to their mineralogical and genetic similarity to the world-class IOCG deposits in north-central Chile including Punta del Cobre, Candelaria, and Manto Verde (Sillitoe and Thompson, 1998). Accordingly, the main ore minerals in the studied tailings were chalcopyrite, pyrite, magnetite, and hematite (Berkh et al., 2019), pointing to the IOCG deposit as the most probable source.

The previously studied tailings exhibited a high bulk Co content with a mean of 845 ppm and a median of 762 ppm. Pyrite was expected to host Co because bulk Co concentrations in subsamples obtained by heavy mineral extraction were directly proportional to the amount of pyrite in the subsamples. Back-scattered electron analysis revealed homogeneous images of pyrite even at the setting of maximum contrast due to minimal density contrasts of Fe and Co. The applied energy dispersive systems including a micro-energy-dispersive X-ray fluorescence microscope (μ-EDXRF) and scanning electron microscope (SEM) were not accurate enough. The reason is an overlapping of Co $K\alpha$ (6.93 KeV) with Fe $K\beta$ (7.06 KeV) caused by the low spectral resolutions of the instruments (145 eV in μ-EDXRF and 130 eV in SEM at Mn $K\alpha$) in the case of low Co concentrations. A longer acquisition time (10 instead 2 ms per pixel) provides distinct Co signals even at small grain sizes but no sharp spatial distribution due to the beam size and sampling depth. Only an electron probe microanalyzer (EPMA) with wavelength-dispersive spectrometry showed that Co is associated with pyrite. However, the EPMA needs a time-consuming sample preparation; thus, it has a long turnaround time for information. Therefore, we tested Raman microprobe analyses to distinguish Co-bearing pyrite from pure pyrite to obtain quick results.

The laser Raman microprobe is a non-destructive and precise method for identification of minerals with a size down to less than 1 μm and can be applied even to samples with rough surfaces. The Raman shift, intensity, width, and number of the Raman bands depend on the nature of the atomic species in the sample and the bond forces between these atoms, as well as the symmetry of their arrangement in the crystal structure. Thus, Raman spectra are unique to a certain type of crystal and can be used to identify samples with unknown mineralogy (Nasdala et al., 2004). Accordingly, modifications of Raman spectra also enable a further characterization such as structural defect, impurity, degree of crystallinity, internal stress, and crystal orientation of the sample being analyzed (Foucher et al., 2017). Since spectra provided by Raman analysis certainly indicate the bonding and symmetry of the mineral structure, polymorphs, e.g., andalusite–sillimanite–kyanite (Mernagh and Liu, 1991), coesite–α-quartz (Nasdala et al., 2004), and pyrite–marcasite (White, 2008), can be distinguished. In comparison to instruments based on electrons or X-ray, Raman spectroscopy can characterize phases containing light elements such as Li minerals (Brooker and Wang, 1992; Anderson et al., 2001). Due to the ability of the laser's penetration into the transparent medium, daughter minerals (precipitated from the fluid after being trapped) in fluid inclusions can also be identified (Mernagh and Trudu, 1993; Kodera et al., 2003).

A group theory treatment of the lattice vibrations in pyrite predicted five Raman active modes including A_g, E_g, and $3T_g$ (Lutz and Willich, 1974). However, three modes including A_g, E_g, and one $T_g(3)$ were observed in most studies (Ushioda, 1972; Macfarlane, 1974; Mernagh and Trudu, 1993; Hope et al., 2001; White, 2008; Pačevski et al., 2008; Kinner et al., 2016; Bryant et al., 2018; Feng et al., 2019; Zhu et al., 2020). Only Vogt et al. (1983) resolved all five modes. Kleppe and Jephcoat (2004) and Yuan and Zheng (2015) measured four out of five modes. The totally symmetric A_g mode is caused by a stretching vibration of the dumbbell S–S bond. The doubly degenerate E_g mode is induced by a libration motion of S displaced perpendicular to the S–S bond axis. The triply degenerate T_g mode involves various stretching and libration modes (Sourisseau et al., 1991). The stretching mode A_g is largely determined by the S–S force

constant, whereas the librational mode E_g and the coupled librational and stretching mode T_g are mainly governed by the Fe–S force constant (Lutz and Zwinscher, 1996).

General Raman studies on pyrite were published by a number of authors (Ushioda, 1972; Macfarlane, 1974; Vogt et al., 1983; Mernagh and Trudu, 1993; Hope et al., 2001; White, 2008; Feng et al., 2019). A high-pressure Raman spectroscopic study of pyrite was carried out by Kleppe and Jephcoat (2004). Yuan and Zheng (2015) also performed high-pressure and high-temperature investigations of pyrite. Bryant et al. (2018) examined a variability in the pyrite spectrum due to laser heating and crystal orientation. However, effects of chemical impurity in pyrite on its Raman spectra have been barely investigated. Rare publications are studies of Cu-bearing pyrite by Pačevski et al. (2008) and As-bearing pyrite by Zhu et al. (2020). Studies on Co-bearing pyrite are also scarce. Only a Raman spectrum for synthetic nanocrystals of $Co_{0.5}Fe_{0.5}S_2$ was recorded by Kinner et al. (2016). To our knowledge, vibrational characterizations of Co-bearing natural pyrite have not been undertaken.

2 Material and analytical techniques

2.1 Sample

Analyzed samples were taken from a tailings dump by drilling up to 7 m. Three drill core samples, M1, M3, and M5, were used in this study. Additionally, the sample "Corte" was collected from the weathered slope of the heap. Generally, the samples M3 and M5 are less weathered than the samples M1 and Corte. Heavy minerals were extracted from the sampled tailings using a shaking table. The extracted heavy mineral concentrates were embedded in epoxy resin, ground with diamond pulley wheel (45 and 15 µm), and polished with diamond paste (3 µm) on cloth. The measurements were always carried out on freshly polished and ethanol-cleaned surfaces. After the cross-sections were studied, they were polished with an Ar broad ion beam (BIB) and re-analyzed for a comparison. Additionally, un-crushed primary rocks supposed to contain Co were collected from a mining site in the vicinity. The rock samples were cut with a diamond-coated saw blade without being polished to avoid a stressed surface because pyrite grains tend to splinter due to the pressure during cutting.

2.2 EPMA

Chemical compositions of pyrite were determined by a field emission microprobe JEOL JXA-8530 F instrument using wavelength-dispersive spectrometry. The point measurements were acquired with a focused beam 0.5 µm in size, an operating voltage of 20 kV, and a beam current of 40 nA. The measured elements and their specification (X-ray line, acquisition time, reference material used for calibration, and calculated detection limit) as follows: S ($K\alpha$, 10 s, pyrite, 200 ppm), Fe ($K\alpha$, 10 s, pyrite, 350 ppm), Co ($K\alpha$, 60 s, cobaltite, 90 ppm), Ni ($K\alpha$, 60 s, pentlandite, 100 ppm), Cu ($K\alpha$, 30 s, chalcopyrite, 160 ppm), As ($L\alpha$, 130 s, cobaltite, 110 ppm), Sb ($L\alpha$, 40 s, stibnite, 160 ppm), and Cd ($L\beta$, 70 s, CdS, 220 ppm). For the semi-quantitative element distribution maps, the same operating conditions were applied. The beam size and dwell time were here 0.5 µm and 1 s, respectively.

2.3 Laser Raman microprobe

The pyrite grains were investigated by a Renishaw inVia Qontor confocal µ-Raman system equipped with a Leica DM2700 microscope. For the polished sample an N plan 100× objective lens with 0.85 numerical aperture and 0.27 mm working distance was used to collect scattered radiation from the sample. For the rough surface of the cut sample an automatic focus track mode and an N plan 20× objective lens with 0.40 numerical aperture and 1.15 mm working distance were applied. A continuous-wave diode-pumped solid-state (CW-DPSS) laser with a wavelength of 532 nm and HeNe laser with a wavelength of 633 nm were used as the excitation source. Unpolarized spectra were recorded by a Renishaw Centrus 1873H8 detector with a charge coupled device (CCD) array of 1040 × 256 pixels using a 1800 L mm^{-1} grating. The spectral resolutions are 1.27 and 0.82 cm^{-1} for the 532 and 633 nm lasers, respectively. Different settings depending on sample, measurement, and laser types were applied and are listed in Table 1.

The instrument was calibrated by automatic alignment procedures of the software WiRE, including laser spot correction, slit, and CCD area alignments. The correctness of the calibration was verified with 520.5 cm^{-1} band of an unprocessed (111) crystalline silicon wafer from First Sensor. The verification is adequate because all Raman modes of pyrite occur between laser line and 520.5 cm^{-1} band of the standard silicon wafer.

The background was subtracted, and spikes caused by cosmic ray events were filtered out from raw spectra. The spectral range of the map measurement was reduced to an area relevant to the pyrite spectrum (250 to 500 Raman shifts per centimeter) to improve the curve fit procedure by avoiding high fluorescence spectra from epoxy resin towards higher wavenumbers. Position, intensity, and full width at half maximum (FWHM) of the Raman bands were determined by the curve fit function of the software. A combined Gaussian–Lorentzian band shape was fitted to the data to minimize the chi-squared (χ^2) value that measures a goodness of fit.

2.4 µ-EDXRF

The element distribution map of the cut sample was acquired by a µ-EDXRF M4 Tornado from Bruker Nano Analytics. A polychromatic excitation emitted by a Rh tube is focused through a polycapillary lens onto a spot size of 17 µm (at Mo

Table 1. Measurement settings.

Sample preparation	Measurement	Objective	Laser (nm)	Power on laser exit slit	Exposure time (s)	Accumulation	Step size (µm)
Mechanical polishing	Map	×100	633	50 % (∼ 9 mW)	1	4	1 × 1
	Map	×100	532	50 % (∼ 26 mW)	1	4	1 × 1
	Point	×100	633	50 % (∼ 9 mW)	30	10	
	Point	×100	532	50 % (∼ 26 mW)	30	10	
	Line	×100	633	50 % (∼ 9 mW)	3	20	
BIB polishing	Map	×100	633	50 % (∼ 9 mW)	1	4	1 × 1
	Point	×100	633	50 % (∼ 9 mW)	30	10	
Cut	Map	×20	532	100 % (∼ 52 mW)	1	1	50 × 50
	Point	×100	633	50 % (∼ 9 mW)	30	10	
	Point	×100	532	50 % (∼ 26 mW)	30	10	

$K\alpha$) and hits the sample. The emitted fluorescence radiation from the sample is detected by a silicon drift detector. 50 keV and 600 µA were applied for the operation of the tube. A step size of 40 µm and a dwell time of 2 ms per pixel were chosen. Chemical compositions of regions of interest (ROI) are calculated as mean spectra by the method of fundamental parameters within the instrument software.

3 Results

3.1 Chemical composition by EPMA

Representative pyrite grains in the extracted heavy mineral concentrates from drill cores M1, M3, and M5 and sample Corte were analyzed by EPMA. The measurement point was usually set in the center but occasionally at the edge of the grains because pyrite grains locally have a As-rich rim with up to 8.7 wt % As. In turn, the center of grains is almost As-free as 3/4 of the analyses fall below the detection limit and 1/4 are below 0.6 wt %. Further impurities including Ni, Cu, Sb, and Cd are under 0.5 wt %, 0.2 wt %, 0.3 wt %, and 0.2 wt %, respectively. Results are listed in Supplement Table S1 and displayed as a circle symbol in Fig. 2. The sample M3 was taken from a less-weathered part of the tailings dump. Additionally, it is coarser grained than others and was thus selected for further analyses. Thereby, line measurements were performed on grains ($n = 7$) containing an elevated concentration of Co. Results are shown as a rectangle in Fig. 2.

Pyrite contains up to 3.8 wt % Co (Fig. 2a). The Co concentration negatively correlates with the Fe concentration. The bigger part of pyrite has a S deficit that results in a low total (Fig. 2b). No correlation between the Fe content and total was observed. Therefore, a low total due to microporosity can be excluded because Fe deficit should proportionally occur at the low total in the case of the microporosity. The relation between stoichiometry and the S content of pyrite is displayed in Fig. 2c. Since As and Sb usually substitute S, whereas Co, Ni, Cu, and Cd replace Fe, the stoichiometry of pyrite is depicted as a ratio (S+As+Sb) at. % / (Fe+Co+Ni+Cu+Cd) at. %. The ratio of all samples is widespread ranging from 1.80 to 2.08 and leads to the gross formula FeS_{2-x} with $-0.07 \leq x \leq 0.20$. Larger deviations from the ideal stoichiometry tend to occur in samples M1 and Corte due to their advanced weathering. Nevertheless, the median values for individual samples including Corte and drill cores M1, M3, and M5 are 1.99, 2.00, 2.00, and 1.98, respectively, which demonstrates a dominance of stoichiometric pyrite.

In Fig. 2d, the Co content expressed as Fe / (Fe+Co) is plotted against stoichiometry. Pure pyrite has a widely dispersed stoichiometry ranging from 1.80 to 2.06, whereas Co-bearing pyrite tends to have a stoichiometry near to 2.00. That means that the stoichiometry is improved by the increasing Co concentration, which can be additionally seen in Fig. 3. Stoichiometry distributions are shown here for pyrite with different Co contents. It is wide in pure pyrite with a standard deviation of 0.035 (Fig. 3a) but narrows with the increasing Co content. The standard deviation decreases hereby up to 0.014 (Fig. 3b–d), and the stoichiometry slightly shifts towards higher numbers. The reason for that is that the Co substitution for Fe is not 1 : 1 (Fig. 2e). According to the trendline equation one Co atom replaces 1.2 Fe atoms, which means that the Co substitution creates vacancies at the Fe position, which raises S to metal ratio and leads to a higher stoichiometry.

3.2 Raman analysis on mechanically polished surface

Raman mapping was performed on seven randomly oriented grains in the coarse-grained and less-weathered sample M3. The selection of the grains was based on an elevated Co concentration. After collecting map spectra, the main E_g and A_g peaks of pyrite were fitted by using the WiRE software. An overlapping of $T_g(1)$ and $T_g(2)$ peaks does not affect the fitted E_g and A_g peaks because their intensity is much weaker than that of the dominant E_g and A_g peaks. $T_g(3)$ peak was

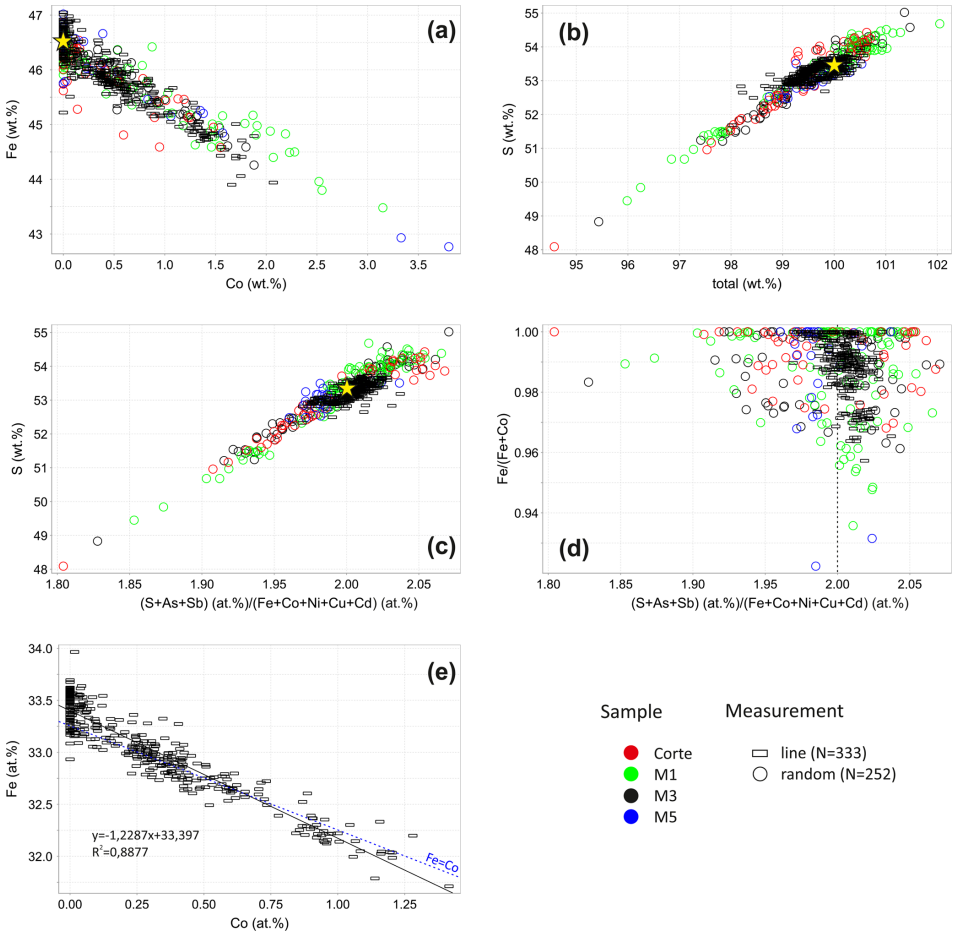

Figure 2. Correlation diagrams for relevant elements of analyzed pyrite grains. Yellow stars and dashed lines pose the theoretical composition of stoichiometric pyrite.

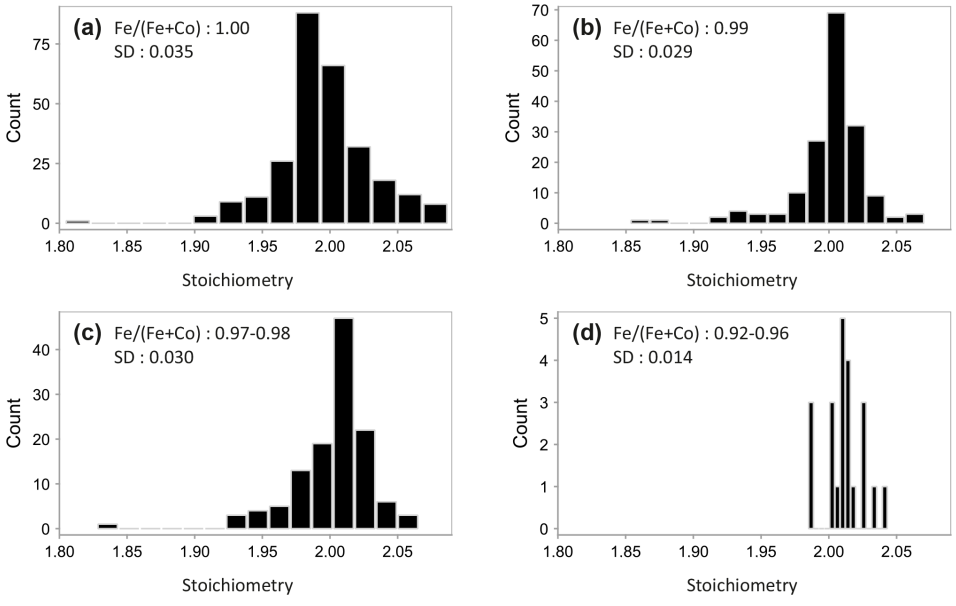

Figure 3. Stoichiometry distributions in four groups of pyrite with differing Co contents.

not fitted because its weakness and large FWHM do not allow for a reliable evaluation. FWHM, Raman shift, and intensity ratio maps of the most representative grain are shown in Fig. 4a–e. The corresponding Co distribution map revealed by EPMA is depicted in Fig. 4f.

Both E_g and A_g modes progressively broaden (Fig. 4a and b) and shift towards lower wavenumbers (Fig. 4c and d) by gaining Co substitution (Fig. 4f). The A_g mode is more sensitive to Co incorporation because its broadness and shifting are stronger compared to the E_g mode. Especially the intensity of the A_g mode drastically drops and diminishes in comparison to the E_g mode. Accordingly, the intensity ratio of the modes (A_g / E_g) decreases with increasing Co concentration (Fig. 4e). It should be noted that limits of the scale are semi-quantitative because they were set visually to attain optimal images.

The grain was additionally mapped by using 532 nm excitation for comparison, and the result is shown in Fig. 5. The pattern of the map is barely changed, proving the same variation of E_g and A_g modes due to the increasing Co concentration independent of the laser energy (Fig. 5a–d). However, the map of the intensity ratio differs (Fig. 5e) because the A_g mode of pure pyrite measured with a 532 nm laser was less intense. Furthermore, a CW-DPSS laser with wavelengths of 1064 nm was tested. Spectra were recorded by an Andor InGaAs detector with a CCD array of 512×1 pixels using an $830\,\mathrm{L\,mm^{-1}}$ grating. The laser was unsuitable because Raman scattering intensity is inversely proportional to λ^4. Accordingly, the only mode existing was a weak A_g mode, and it disappeared as soon as pyrite had a trace amount of Co.

The grain was examined with reflected light microscopy. Under reflected and parallel-polarized light, the grain is homogeneous and possesses no pleochroism. Under nearly cross-polarized light, two domains with a weak anisotropy were observed (Fig. 6). They alternately become extinct during rotation of the microscope stage, which demonstrates the presence of two domains of different lattice orientation. One belongs to pure pyrite, and the other one belongs to the surrounding Co-bearing pyrite that hosts several sectors seen in both Raman and element distribution maps (Fig. 4). The weak anisotropy usually points to a distortion of the lattice and is therefore most probably the result of a surface deformation due to the mechanical polishing procedure (Libowitzky, 1994).

3.3 Element distribution map: comparison of Raman signature and Co content of pyrite along line measurements

An enlarged semi-quantitative element distribution map of the investigated grain is shown in Fig. 7. The limits of the scale bar correspond to maximum and minimum values obtained by the line measurement on the grain. Sector I presents pure pyrite. The remaining sectors including II, III, IV, and V have increasing Co concentrations up to 1.2 at. %.

Sector I presents the first generation of pyrite and has a concentric growth zoning caused by a trace amount of Co. The margin of the sector shows increased but strongly variable Co contents. Sectors IV and V pose the second generation of pyrite and have a tabular-like habitus. Sector IV has a lower Co content than sector V and therefore may present a leached part of the second generation. Sectors II and III demonstrate the last generation of pyrite that deposited in interstitial volumes and has a collomorph-banded-like texture. The contact between the three generations is distinct and sharp implying a presence of different crystal domains. However, only the first generation has a different crystal orientation, while the last two generations show the same crystal orientation because they uniformly darken during rotation of the microscope stage under reflected and nearly cross-polarized light (Fig. 6). Therefore, it seems to be a crystallographically oriented intergrowth or recrystallization.

As mentioned, the A_g mode is more sensitive to the varying Co content, especially its intensity. Thus, the intensity of the mode is quantitatively compared with the Co content by collecting 32 Raman and EPMA point measurements indicated by the red line in Fig. 7. Results are displayed below the element distribution map (Fig. 7) and listed in Supplement Table S2. The line was chosen by eye in both methods. Therefore, a minor spatial discrepancy can occur, which might lightly affect the comparison diagrams. The measurement number 22 is omitted because it was acquired in a fracture.

The intensity of the A_g mode varying from 3357 to 17 050 is strongly influenced by the small amount of Co up to 1.2 at. %. The more Co in pyrite there is, the lower the intensity of the A_g mode will be. The reciprocal correlation is almost linear except for sector III containing a trace amount of Co ranging from 0.2 at. % to 0.5 at. %. The intensity of the A_g mode shows here a stronger dip implying that incorporation of trace Co results in an abrupt change in the dumbbell S–S bond. Similarly, Yuan and Zheng (2015) observed that the chemical bonds of pyrite are more sensitive to stress changes at low pressures than at high pressures. Differences in crystal lattice orientation between different sectors could be responsible for some of the variation in the intensity of the A_g mode, as noted in Bryant et al. (2018). However, sector III has the same crystal orientation as sectors II, IV, and V, as noted previously. Stoichiometry does not play a role in the intensity of the A_g mode because there is no correlation. The stoichiometry is here expressed as ratio S / (Fe+Co) since other impurities were negligible. The ratio weakly deviates from an ideal straight line and varies between 1.99 and 2.04, pointing to a nearly stoichiometric pyrite. The noticeable dip in the intensity of the A_g mode occurs above 0.2 at. % Co. Thus, 0.2 at. % can be regarded as a detection limit of the Raman technique for Co.

Point measurements with longer acquisition time were performed for sectors I–V. The data were collected from a pixel of the Raman map showing the most optimal spectrum

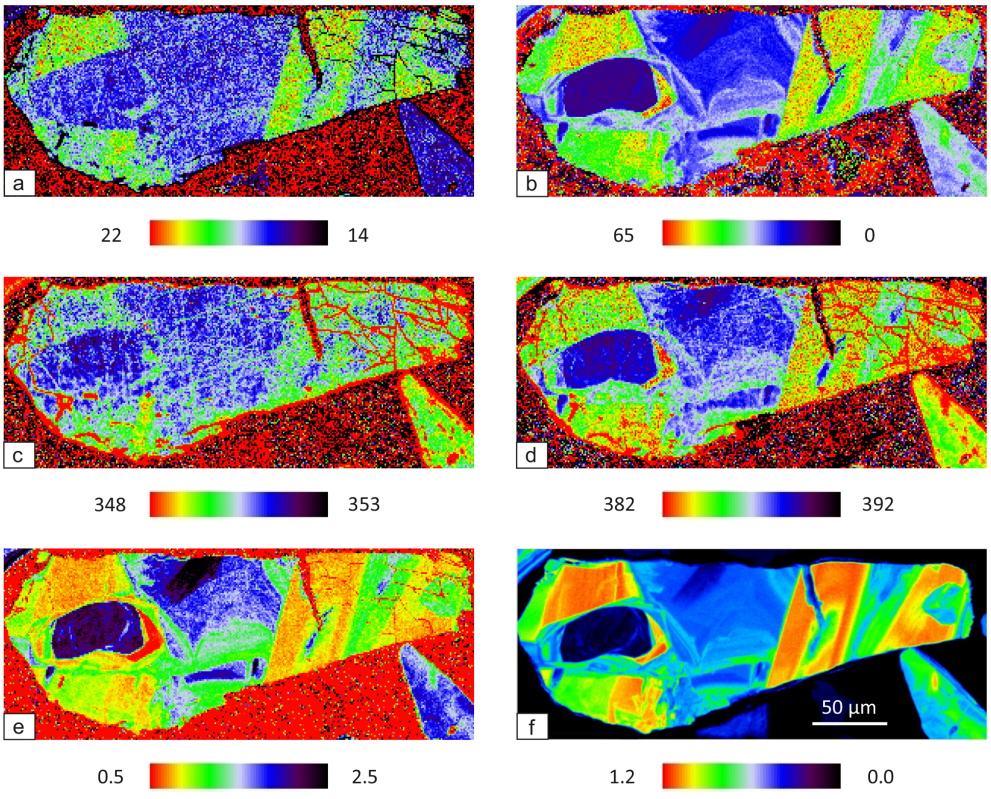

Figure 4. Raman map of pyrite grain with 633 nm laser. FWHM of E_g **(a)** and A_g **(b)** modes (presented in cm^{-1}), Raman shift of E_g **(c)** and A_g **(d)** modes (presented in cm^{-1}), intensity ratio of E_g and A_g (A_g / E_g) modes **(e)**, and Co distribution map revealed by EPMA (presented in at. %) **(f)**.

with a high signal-to-noise ratio. The positions of the acquired spectra approximately correspond to the positions of the numerals in Fig. 7. The Raman shifts, FWHM, and intensity ratios of the main E_g and A_g modes are listed in Table 2 in addition to literature data.

Spectra revealed by the 532 and 633 nm lasers are comparable (Fig. 8). The peak centers of the E_g and A_g modes are 351 and 387 cm^{-1} with the 532 nm laser and 351 and 388 cm^{-1} with the 633 nm laser. The corresponding FWHM of the E_g and A_g modes are 16.1 and 16.4 cm^{-1} with the 532 nm laser and 17.0 and 14.0 cm^{-1} with the 633 nm laser. Regardless of the laser type, both the E_g and A_g modes progressively shift to lower wavenumbers and broaden as the Co concentration is increased. Furthermore, the intensity of the A_g mode decreases. A remarkable difference between spectra collected by the two lasers is the more intense A_g mode and its stronger diminishment with the 633 nm laser. Generally, the 633 nm laser is more suited for Co evaluation because the change in the spectra due to the varying Co substitution is more prominent.

However, our spectra of pure pyrite disagree with most of the data published previously (Table 2). Generally, Raman spectra of pyrite in the literature are markedly variable since numerous factors such as crystal orientation, laser energy, and in particular chemical impurity and sample preparation have a strong influence on spectra.

Unpolished samples typically possess inadequate quantitative chemical information since common in situ methods require a polished surface. Accordingly, it is unknown whether their Raman spectra have been affected by impurities or not. In turn, studies performed on polished samples offer chemical information but reveal increased band frequencies and widths similar to our results. Since a surface deformation of pyrite was predicted under reflected and parallel-polarized light as a weak anisotropy, we assume that such biased spectra are the result of the mechanical polishing. Thus, a BIB polishing technology was applied to eliminate the surface strain. Subsequently, the sample was re-analyzed by the Raman method.

3.4 Raman analysis on broad ion beam polished surface

Raman mapping was performed in an area within the grain previously analyzed. The same measurement settings and fitting procedure were applied. FWHM, Raman shift, and intensity ratio maps are shown in Fig. 9a–e. The corresponding spectra collected from available sectors by point measure-

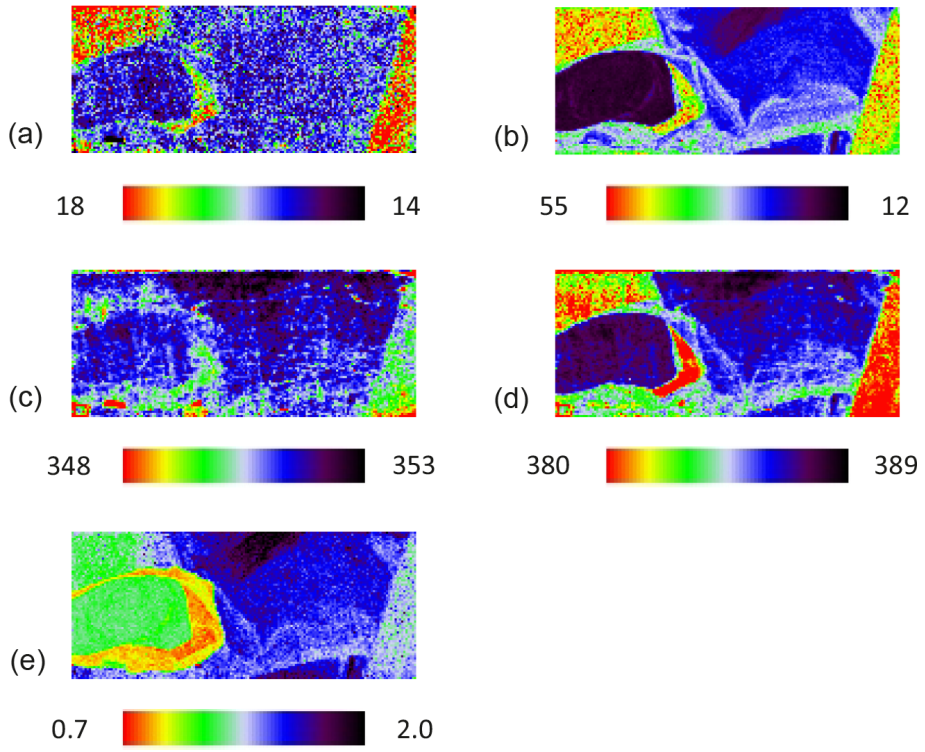

Figure 5. Raman map of pyrite grain with 532 nm laser. FWHM of E_g **(a)** and A_g **(b)** modes (presented in cm^{-1}), Raman shift of E_g **(c)** and A_g **(d)** modes (presented in cm^{-1}), and intensity ratio of E_g and A_g (A_g / E_g) modes **(e)**.

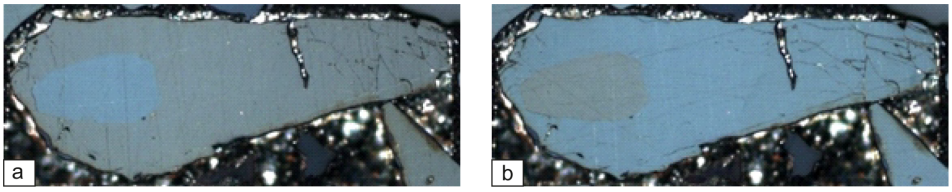

Figure 6. Pyrite grain under reflected and nearly cross-polarized light positioned at 0° **(a)** and rotated by 90° **(b)**.

ments are shown in Fig. 9f, and results of the peak fitting procedure are listed in Table 3.

The pattern of the map has scarcely changed, proving the same variation of E_g and A_g modes due to the increasing Co concentration independent of the sample preparation. Similar to former results the A_g mode broadens and shifts stronger than the E_g with the Co concentration. The intensity ratio of the modes (A_g / E_g) also decreases, but it is lower than that before BIB polishing. The reason could be a trace amount of Co at the changed level of the grain surface after BIB polishing.

A distinct difference to the previous spectra is that the current spectra exhibit much narrower Raman modes located at lower frequencies (Fig. 9f and Table 3), showing that the stressed surface has been abraded by the BIB. Due to the reduced FWHM of the modes the $T_g(1)$ mode could be separated. Like with others the $T_g(1)$ mode shifts to lower wavenumbers and broadens with the increasing Co content. For the Co-bearing pyrite more than four peaks were fitted to reduce χ^2 values. The final χ^2 values were 0.01, 0.03 and 0.03 for pyrite in sectors I, III, and V, respectively. The curve fitting results are depicted in Supplement Fig. S2. The Co incorporation obviously generates additional unidentified broad bands in the spectrum of Co-bearing pyrite ("?" in Table 3). They are located at 376 and 397 cm^{-1} for sector III and at 361, 374, and 397 cm^{-1} for sector V.

3.5 Raman analysis on cut surface

A cut of hand specimen (Fig. 10a) was investigated according to its chemical composition using a µ-EDXRF. The obtained element distribution map is shown in Fig. 10b. Relevant elements including S, Co, Fe, Cu, and Si are presented in false colors.

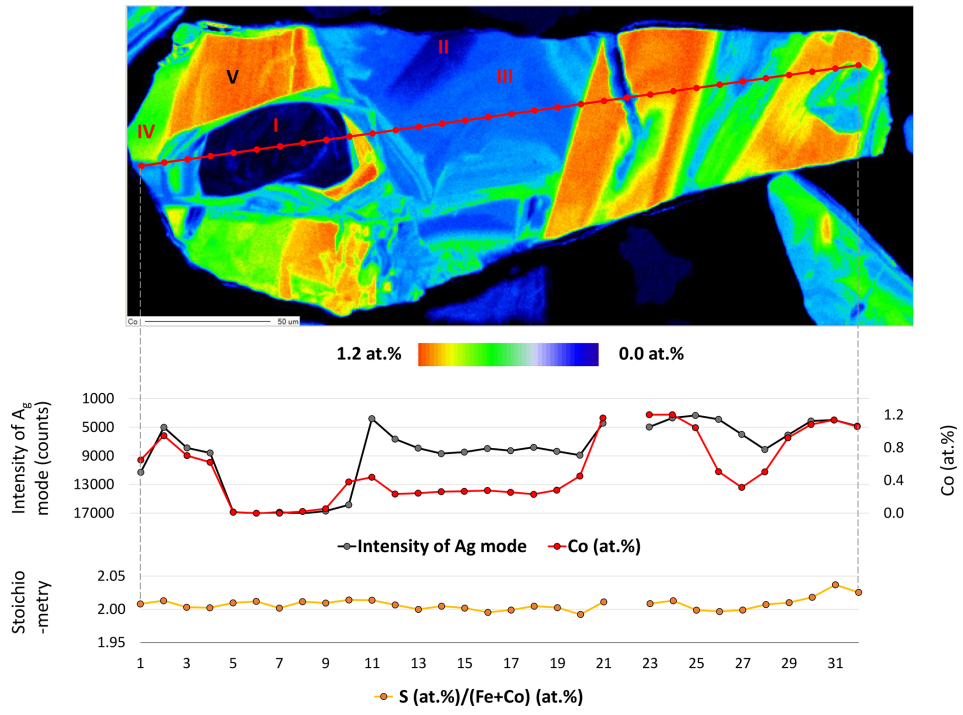

Figure 7. Semi-quantitative Co distribution map of pyrite and position of quantitative analyses along the red line performed by microprobe and Raman spectroscopy. Results are presented in the diagram below the map. Numbers (I–V) on the map present positions of Raman spectra acquired by point measurements.

The rock is composed mainly of magnetite (blue) and quartz (black) and hosts veinlets consisting of chalcopyrite (yellow), pure pyrite (magenta), and Co-bearing pyrite (cyan). Chalcopyrite and pure pyrite appear to have coevally mineralized first. Then Co-bearing pyrite filled the remaining pore spaces of the veinlets or a Co-bearing fluid interacted with preexisting pure pyrite and replaced Fe with Co. A small amount of calcite, pyroxene, amphibole, and chlorite is also present in the host rock.

Up to ± 1.5 at. % Co was measured in pyrite. However, the real maximum content should be higher because concentrations were calculated as a mean spectrum of an ROI that usually consists of several sectors with varying Co concentrations as seen in the element distribution map by EPMA (Fig. 7).

Raman mapping was performed in an area within the red square in Fig. 10b using 532 nm laser. The same fitting procedure as used for the polished samples was applied. FWHM, Raman shift, and intensity ratio maps are shown in Fig. 11a–e. The corresponding enlarged element distribution map is depicted in Fig. 11f. Single point spectra acquired from pure and Co-bearing pyrite using 532 and 633 nm lasers are presented in Fig. 11g and h. Results of the peak fitting procedure are listed in Table 4.

Similar to previous results the E_g mode is rather insensitive and barely changes with the Co incorporation (Fig. 11a and c). Red pixels here belong to chalcopyrite and magnetite and can be ignored. As expected, the A_g mode broadens (Fig. 11b) and shifts with elevating Co concentration (Fig. 11d); also the intensity ratio of the modes (A_g / E_g) decreases (Fig. 11e).

Spectra collected from the cut surface by point measurement are comparable to those from the BIB polished surface. The modes are sharp and located at lower frequencies (Table 4). The $T_g(1)$ mode is present owing to the reduced FWHM of the modes. For Co-bearing pyrite extra peaks were fitted to reduce χ^2 values. The final χ^2 values were less than 0.03. The modification of the pyrite spectra due to the Co substitution is independent of the laser wavelengths. The only difference is the narrower bandwidths achieved by the 633 nm laser due to higher spectral resolution.

4 Discussion

4.1 Pyrite chemistry

Since pyrite is a refractory mineral that is stable up to relatively high temperatures, it readily preserves trace element signatures. Thus, the trace element geochemistry of this ubiquitous mineral can be used as a geochemical tool in ore genesis (Cook et al., 2016). In particular, the Co/Ni ratio in mineralizing fluid can be preserved in pyrite as both elements are usually incorporated equally due to their similarity. Pyrites formed at or below the seafloor in sedimen-

Table 2. Comparison of investigated and literature wavenumbers (cm^{-1}) for Raman spectrum of pyrite. $T_g(1)$ and $T_g(3)$ modes are not presented.

E_g		A_g		A_g / E_g	Chemical	Laser	Sample	Locality	Source
Center	FWHM	Center	FWHM	intensity	composition		preparation		
351	18.0	385	15.0	3.8–1.0*	–	454.2–514.5	Polished	–	Macfarlane et al. (1974)
351	2.4	385	1.7		–	454.2–514.5	Unpolished	–	Macfarlane et al. (1974)
343	4.7	379	5.7*	4.3*	–	514.5	Polished	East Tirol, Italy	Vogt et al. (1983)
353	–	374	–	–	–	–	–	–	Sourisseau et al. (1991) calculated
353	16.0*	387	17.0*	0.8*	< 5 % impurity	514.5	–	Guinaoang, northwestern Luzon, Philippines	Mernagh and Trudu (1993), pyrite isotropic
342	7.4*	377	8.5*	1.5*	< 5 % impurity	514.5	–	Pine Creek, N.T., Australia	Mernagh and Trudu (1993), pyrite anisotropic
342	9.2*	377	8.5*	7.9*	–		–	–	Hope et al. (2001)
344	3.2	379	4.5	2.3*	–	514.5	–	–	Kleppe and Jephcoat (2004)
343	10.5	379	10.5	1.1*	–	532	Unpolished	Inactive chimney from 11° N on the East Pacific Rise	White (2008)
336–346	9.7–32.2	377–383	10.3–29.6	–	< 8 wt % Cu	785	Polished	Čoka Marin, Serbia	Pačevski et al. (2008)
331–343	2.3–22.6	376–379	0.3–20.7	–	< 8 wt % Cu	785	Alkaline silica	Čoka Marin, Serbia	Pačevski et al. (2008)
336–347	14.5–27.8	373–384	16.8–27.0	1.3* (Cu-poor), 1.0* (Cu-rich)	< 8 wt % Cu	633	Polished	Čoka Marin, Serbia	Pačevski et al. (2008)
344	3.9	380	3.9	0.9*	–	514.5	Unpolished	–	Yuan and Zheng (2015)
341	11.4*	377	11.4*	1.0*	Pure Fe_2S	633	Nanocrystals	Synthetic	Kinner et al. (2016)
321	38.6*	376	50.0*	0.9*	Pure Co_2Fe_2S	633	Nanocrystals	Synthetic	Kinner et al. (2016)
342–343	4.4–5.1	378–379	4.4–30.0	1.0 on (100) 1.8 on (111) 1.4 on (210)	< 0.1 wt % Ni < 1 wt % As	532	Unpolished	Several localities	Bryant et al. (2018)
342	6.2*	380	6.2*	2.3* on (100) 4.2* on (110) 5.1* on (111)	0.1 wt % Zn	532	Polished	Hunan Province, China	Feng et al. (2019)
351	17.0	388	14.0	2.0	∼ 0.0 at. % Co	633	Polished	North-central Chile	This study, sector I
351	18.6	389	17.5	2.0	∼ 0.2 at. % Co	633	Polished	North-central Chile	This study, sector II
350	18.5	386	22.9	1.3	∼ 0.4 at. % Co	633	Polished	North-central Chile	This study, sector III
349	20.2	384	31.5	0.8	∼ 0.6 at. % Co	633	Polished	North-central Chile	This study, sector IV
343	18.3	373	46.2	0.5	∼ 1.2 at. % Co	633	Polished	North-central Chile	This study, sector V
351	16.1	387	16.4	1.2	∼ 0.0 at. % Co	532	Polished	North-central Chile	This study, sector I
351	16.0	386	19.1	1.8	∼ 0.2 at. % Co	532	Polished	North-central Chile	This study, sector II
351	16.5	384	34.9	1.5	∼ 0.4 at. % Co	532	Polished	North-central Chile	This study, sector III
348	19.3	380	35.4	1.3	∼ 0.6 at. % Co	532	Polished	North-central Chile	This study, sector IV
346	19.0	374	39.3	0.9	∼ 1.2 at. % Co	532	Polished	North-central Chile	This study, sector V

* The present authors determined FWHM and intensity ratios by manually measuring enlarged spectra if not clearly reported. – Not reported.

Table 3. Frequencies and FWHM of observed Raman modes of pyrite measured on BIB polished surface (cm^{-1}).

Sect.	E_g		$T_g(1)$		?		A_g		?		?		$T_g(3)$		A_g / E_g
	Center	FWHM	Center	FWHM	Center	FWHM	Center	FWHM	Center	FWHM	Center	FWHM	Center	FWHM	
I	342	2.6	349	3.2			378	3.0					429	4.5	0.9
III	342	3.1	348	3.0			376	3.3	376	15.0	397	31.9	428	5.2	0.4
V	339	5.4	345	4.0	361	20.1	373	5.1	374	41.5	397	8.8	423	9.1	0.1

Table 4. Frequencies and FWHM of observed Raman modes of pyrite measured on cut surface (cm^{-1}).

Sector	Laser	E_g		$T_g(1)$		?		A_g		?		$T_g(3)$		A_g / E_g
	(nm)	Center	FWHM	Center	FWHM	Center	FWHM	Center	FWHM	Center	FWHM	Center	FWHM	
Pure	532	343	3.0	350	3.4			379	5.5			430	4.6	1.2
Pure	633	343	2.6	350	2.5			379	5.0			431	4.2	1.7
Co	532	342	4.1	348	3.8	375	21.3	376	5.8			427	5.6	0.3
Co	633	342	3.5	348	3.8	373	25.1	376	3.3	400	16.3	427	5.6	0.3

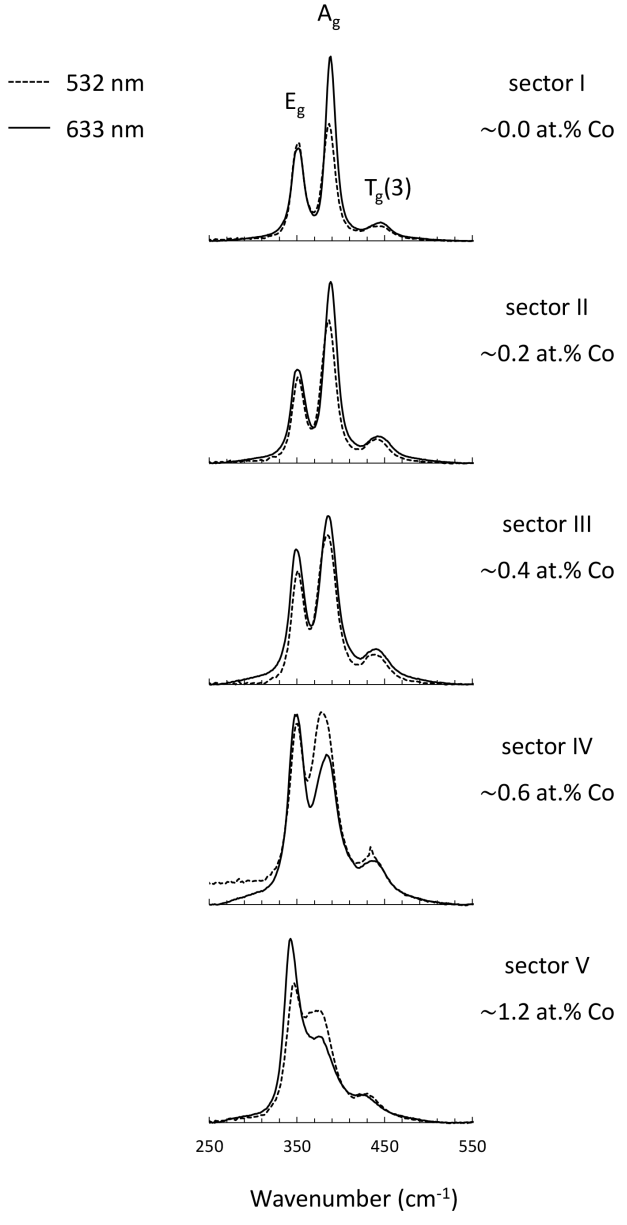

Figure 8. Raman spectra of pyrite with varying Co contents by 532 and 633 nm lasers.

tary and volcanic settings are generally characterized by low Co/Ni ratios (< 1), whereas magmatic–hydrothermal pyrite exhibits Co/Ni ratios between ~ 1 and 10 (del Real et al., 2020). Pyrite in our study is considered to be hydrothermal and was deposited in the Mantos de Punitaqui vein. However, it has highly variable Co/Ni ratios ranging from nearly 0 to over 100 caused by very low Ni concentrations. For such a high ratio a metamorphic event might be responsible as metamorphism leads to a loss of Ni and gain of Co (Bralia et al., 1979).

Grain-scale heterogeneity in our sample is primarily the result of different generations of pyrite, indicating multiple pulses of the mineralizing fluid. The fine chemical zoning due to Co incorporation within a single generation is in turn most probably caused by temperature fluctuations of the host fluid, at least at a local scale. Numerous studies have shown that Co incorporation into pyrite tends to be more efficient under higher-temperature conditions (del Real et al., 2020; Grant et al., 2018).

Other geochemically important trace elements are, for example, temperature- and redox-sensitive pairs such as Se and Ni (del Real et al., 2020). However, their concentrations in our pyrite sample are nearly always below the detection limits of EMPA. Therefore, laser ablation inductively coupled plasma mass spectrometry (LA-ICP-MS) would help to record such low concentrations. The method has recently been widely applied for elemental mapping of pyrite to study ore formation (Cook et al., 2016; del Real et al., 2020; Zhou et al., 2017). However, this is a destructive technique with a relatively large ablation crater for a moderately hard mineral like pyrite, which can be 20 µm deep, giving an ablated volume of several thousand cubic micrometers (Cook et al., 2016). This makes it difficult to perform a correlative study with Raman techniques with a spot size of less than 1 µm, especially for minerals with micro-scale compositional zonation such as pyrite in this study.

4.2 Band position

The Raman band position of pyrite normally depends on pressure and temperature change (Kleppe and Jephcoat, 2004; Yuan and Zheng, 2015). Laser heating at the sample surface causes downshifting of bands (Bryant et al., 2018). In our case, the effect of laser heating due to longer exposure time was small because the spectra extracted from the

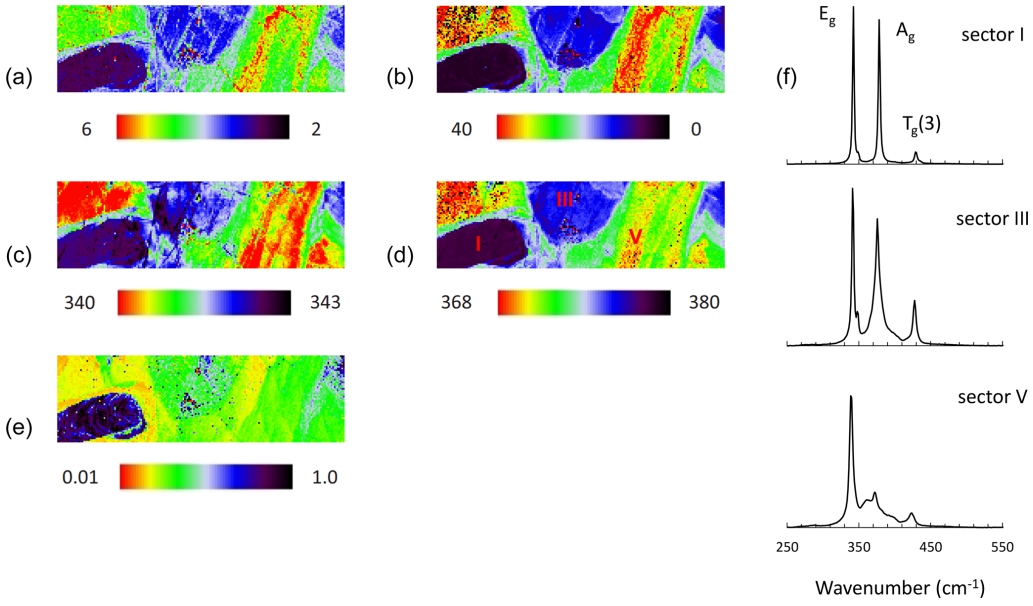

Figure 9. Raman map of pyrite grain with 633 nm laser after BIB polishing. FWHM of E_g **(a)** and A_g **(b)** modes (presented in cm^{-1}), Raman shift of E_g **(c)** and A_g **(d)** modes (presented in cm^{-1}), intensity ratio of E_g and A_g (A_g / E_g) modes **(e)**, and Raman spectra of pyrite collected from sectors I, III, and V by point measurements **(f)**.

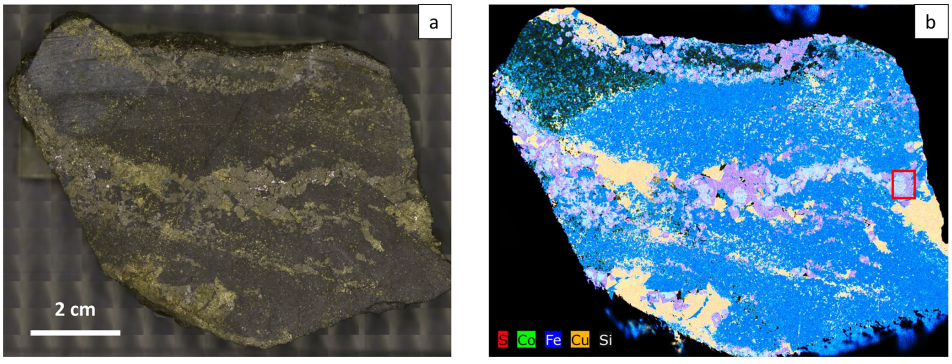

Figure 10. Cut of rock sample **(a)** and element distribution map revealed by µ-EDXRF **(b)**.

map with an exposure time of 4 s per pixel were comparable to the point measurements with a longer exposure time of 5 min (Table 3 and Fig. 9). Zhu et al. (2020) reported a notable downshift of band positions of up to 7 cm^{-1} at the higher laser power of 75 mW instead of 1.5 mW in As-rich pyrite (up to 4.9 wt % As). Similarly, we observed a downshifting of the A_g band by up to 4 cm^{-1} when the laser power was increased from 0.5 to 52 mW in pure pyrite, as well as in Co-bearing pyrite (Supplement Fig. S3). Moreover, a regular mechanical polish led to strongly upshifted bands, which could be avoided by analyzing BIB polished or cut surfaces.

In this study, the downshifting of the modes is caused by Co substitution because the laser power was kept constant during measurements. Cattierite (CoS_2) readily forms a solid solution series with pyrite (Klemm, 1965; Bouchard, 1968). The lattice constant of cattierite is 5.53 Å (Pratt and Bayliss, 1979; Kwon et al., 2000), whereas it is 5.42 Å in pyrite. Gaining lattice constants with an increasing Co concentration in synthetic nanocrystals of pyrite was predicted, as well as measured, by Kinner et al. (2016). It confirms our observation that both E_g and A_g modes downshift with increasing Co content, implying a lengthening of chemical bonds which reflects an expansion of the crystal structure. Fujioka et al. (2016) also observed a downshifting of frequencies by a substitution of Co in $NiTiO_3$. Their interpretation was an average symmetry lowering through a structural distortion. However, pure cattierite has a fairly different Raman spectrum than that of pyrite, although they have the same structure type. According to the RRUFF database, the strongest mode of cattierite is at 385 cm^{-1}, and the second strongest mode is at 291 cm^{-1}.

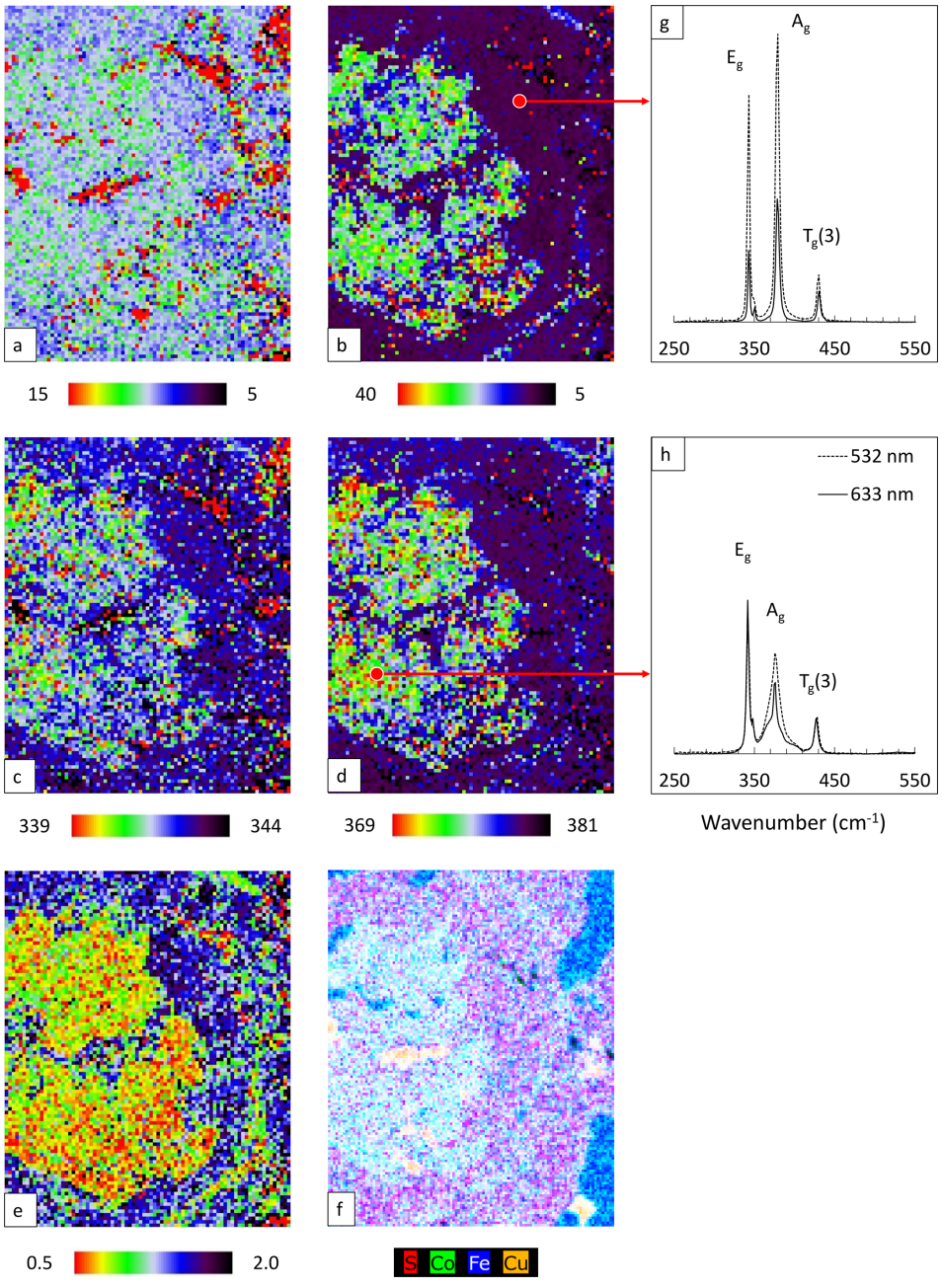

Figure 11. Raman map of pyrite grain with 532 nm laser. FWHM of E_g **(a)** and A_g **(b)** modes (presented in cm^{-1}), Raman shift of E_g **(c)** and A_g **(d)** modes (presented in cm^{-1}), intensity ratio of E_g and A_g (A_g / E_g) modes **(e)**, element distribution map revealed by μ-EDXRF **(f)**, and Raman spectra of pure pyrite **(g)** and Co-rich pyrite **(h)**.

The A_g mode of pyrite is more sensitive and displays stronger downshifts than the E_g mode. It might be explained by the following. The longer the S–S distance is, the shorter the M–S distance is in FeS_2, CoS_2, and NiS_2. The sum of the two bond lengths remains nearly constant (Elliott, 1960). The A_g mode is largely determined by the S–S force constant, whereas the E_g mode is mainly governed by the Fe–S force constant (Sourisseau et al., 1991; Lutz and Zwinscher, 1996). Therefore, during the expansion of the unit cell due to the Co substitution, the downshifting of the E_g mode is weaker than the A_g mode.

4.3 Bandwidth

Increasing the laser power from 0.5 to 52 mW resulted in a slight broadening of A_g band by up to 1 cm^{-1} in both pure and Co-bearing pyrites (Supplement Fig. S3). In turn,

the bandwidths are extremely sensitive to surface strains. A rough polishing with 3 µm diamond paste resulted in strongly broadened bandwidths ranging from 14 to 17 cm^{-1} for pure pyrite, whereas they were less than 2.6 cm^{-1} when measured from a BIB polished or cut surface. Pačevski et al. (2008) also achieved a reduced FWHM with a chemo-mechanical final polish.

The increasing bandwidths with the elevating Co content in this study is caused by an overlap of several Raman bands. Pyrite is a natural semiconductor with an indirect band gap of $\sim$0.95 eV (Ferrer et al., 1990) that can be significantly decreased by Co substitution (Xian et al., 2012). The decrease in the band gap strongly affects the electrochemical properties of the mineral and accordingly vibrational properties of the crystal. The formation of additional bands may also hint at a structural disorder because the chemical analyses on pyrite predict a creation of vacancies at the Fe position due to Co substitution. Similarly, Fujioka et al. (2016) demonstrated a structural distortion by the substitution of Co in $NiTiO_3$, but the Raman modes in their study remained sharp. The explanation was a homogeneous spatial Ni/Co ratio within a laser spot implying a long-range structural disorder (Fujioka et al., 2016). In turn, the Co distribution in pyrite in our case appears to be rather heterogeneous at the nanoscale level, hinting at a short-range, as well as long-range, structural distortion.

4.4 Intensity of band

The ratio of band intensities is usually affected by the crystal lattice orientation with respect to the laser's dominant polarization plane (Vogt et al., 1983; Bryant et al., 2018; Feng et al., 2019). Thus, different lattice orientations of the analyzed pyrite grains are responsible for some of the variation in the A_g mode intensity. Although the mapped grains were randomly oriented (Supplement), the representative grain studied contained several sectors with different crystal orientations (Fig. 6), and the analyzed area of the cut sample consisted of several subgrains (Fig. 11); a similar observation, which is that the intensity of the A_g mode decreases with increasing Co concentration in pyrite, was made in all cases.

A resonance effect depending on excitation energy also enhances the intensity of certain bands, which changes the intensity ratio of the bands. Macfarlane et al. (1974) observed a progressive gain in the intensity ratio (A_g / E_g) from 1 to 4 on tuning the incident Ar^+ laser energies from 2.41 to 2.73 eV. They suggested that the resonance Raman scattering in pyrite is mostly contributed by two direct inter-band electronic transitions occurring at 2.47 and 2.85 eV. Kleppe and Jephcoat (2004) also observed a resonance scattering of A_g and $T_g(1)$ modes with increasing pressure.

Similar to pure pyrite in this work, almost all pyrites in the literature that are supposed to be pure have a stronger A_g mode than E_g mode (Table 2). Thus, the diminishing of the A_g mode correlating to increasing Co concentration is caused by the Co substitution itself. It partly results from the splitting out of the $T_g(2)$ mode from the A_g mode but not completely because the $T_g(2)$ mode is less intense than $T_g(3)$ mode (Vogt et al., 1983), and its subduction would not result in such a strong decrease. Thus, some kind of Co-induced "antiresonant scattering" of the A_g mode seems to be the reason.

Finally yet importantly, chemical impurity affects all three signatures. However, a chemical investigation of the analyzed pyrite was neglected in a number of publications (Table 2), which can highly modify the pyrite spectra as seen in this study.

4.5 Similar cases

Hope et al. (2001) and Osadchii and Gorbaty (2010) observed in case of sphalerite that the intensity of the LO (longitudinal optical) mode at 350 cm^{-1} decreases, whereas the TO (transverse optical) mode at 275 cm^{-1} became more intense when the mineral contained more Fe. Pačevski et al. (2008) also recorded a correlation between increasing Cu content up to 8 wt % and decreasing band position and increasing bandwidth in natural pyrite (inferred to be in solid solution). These authors explained that the pyrite structure is slightly expanded due to the larger Cu atoms, and thus the bonds become longer and weaker. Additionally, distorted Cu sites result in a variety of structural environments in the lattice and consequently broadening of bands. Furthermore, intensities of the E_g and A_g modes were approximately equal in Cu-rich zones, whereas the intensity of A_g was higher in Cu-poor zones. Zhu et al. (2020) also recognized a strong linear correlation between As content and band positions of pyrite. All three Raman bands were shifted downwards (up to 10 cm^{-1}) with an increase in As content from below 0.05 wt % to 4.89 wt %. The authors concluded that the downshifting was due to increased bond lengths and local distortions within an expanded crystal structure.

A Raman spectrum for synthetic nanocrystals of $Co_{0.5}Fe_{0.5}S_2$ was recorded by Kinner et al. (2016). The spectrum differed from a simple combination of Raman spectra obtained from the CoS_2 and FeS_2, indicating the stoichiometric substitution of Co^{2+}. The E_g and A_g modes of $Co_{0.5}Fe_{0.5}S_2$ were downshifted from those of FeS_2 (Table 2). The bandwidths were also strongly broadened, but the intensity ratio remained constant (Kinner et al., 2016).

5 Conclusions

We have determined the effect of Co substitution in pyrite on Raman spectra of the mineral. A trace amount of Co causes a downshifting and widening of the Raman bands, as well as diminishment of the A_g band of pyrite. The noticeable dip in the intensity of the A_g band occurs above 0.2 at. % Co, which can be regarded as a detection limit of the Raman

technique. We have also observed that the sample preparation has a strong influence on the pyrite spectra. The standard mechanical polishing resulted in strongly broadened modes at upshifted frequencies, which could be avoided by analyzing BIB polished or cut samples. However, the effect of Co on pyrite spectra is independent of the sample preparation, enabling the method as a possible tool for the differentiation of Co-bearing pyrite from pure pyrite. Raman spectroscopy has several advantages over other methods. There is no need of sample preparation due to a unique application in the rapid focusing on a rough surface even for crushed ores. No vacuum chamber and wavelength-dispersive analysis are necessary.

Assaying of ore prior to crushing and subsequent separation of Co-rich ore would help to ensure that this strategic element is recovered as a by-product rather than ending up in the tailings pile. In addition, the separation would help to reduce the volume of acid-generating mine tailings. Since pyrite is a natural semiconductor and its electrochemical properties can be modified by a Co substitution, quantitative Raman analyses for composition and qualitative analyses for crystallinity, strain, and stress of the Co-doped pyrite can be interesting for the semiconductor industries. Lastly, nondestructive and micro-Raman mapping technique could have important applications in the study of ore genesis.

Data availability. All raw data can be provided by the corresponding author upon request.

Supplement. The supplement related to this article is available online at: https://doi.org/10.5194/ejm-34-259-2022-supplement.

Author contributions. KB performed the data collection and evaluation. KB wrote the manuscript with input from DR. Both authors discussed and interpreted the results.

Competing interests. The contact author has declared that neither they nor their co-author has any competing interests.

Disclaimer. Publisher's note: Copernicus Publications remains neutral with regard to jurisdictional claims in published maps and institutional affiliations.

Acknowledgements. We thank Simon Goldmann and Christian Wöhrl for excellent support during the EPMA, Dominic Göricke for great technical support, Donald Henry and Antoine Fourrière for sample preparation, and Malte Drobe for providing rock samples at the Federal Institute for Geosciences and Natural Resources. We also thank anonymous reviewers and the editor for their insightful comments and suggestions and Allen Nutman at the UOW for an invaluable consultation.

Financial support. This research was funded by the German Mineral Resources Agency under the grant number A-0203006.A.

Review statement. This paper was edited by Etienne Balan and reviewed by two anonymous referees.

References

Anderson, A. J., Clark, A. H., and Gray, S.: The occurrence and origin of zabuyelite (Li_2CO_3) in spodumene-hosted fluid inclusions: Implications for the internal evolution of rare-element granitic pegmatites, Can. Mineral., 39, 1513–1527, https://doi.org/10.2113/gscanmin.39.6.1513, 2001.

Berkh, K., Rammlmair, D., Drobe, M., and Meima, J.: Case Study: Geochemistry and Mineralogy of Copper Mine Tailings in Northern Central-Chile, ICAM, 14, 37–40, https://doi.org/10.1007/978-3-030-22974-0_9, 2019.

Bouchard, R. J.: The preparation of pyrite solid solutions of the type $Fe_xCo_{1-x}S_2$, $Co_xNi_{1-x}S_2$, and $Cu_xNi_{1-x}S_2$, Mater. Res. Bull., 3, 563–570, https://doi.org/10.1016/0025-5408(68)90087-1, 1968.

Bralia, A., Sabatini, G., and Troja, F.: A revaluation of the Co/Ni ratio in pyrite as geochemical tool in ore genesis problems, Miner. Deposita, 14, 353–374, https://doi.org/10.1007/BF00206365, 1979.

Brooker, M. H. and Wang, J.: Raman and infrared studies of lithium and cesium carbonates, Spectrochim. Acta A.-M., 48, 999–1008, https://doi.org/10.1016/0584-8539(92)80176-W, 1992.

Bryant, R. N., Pasteris, J. D., and Fike, D. A.: Variability in the Raman Spectrum of Unpolished Growth and Fracture Surfaces of Pyrite Due to Laser Heating and Crystal Orientation, Appl. Spectrosc., 72, 37–47, https://doi.org/10.1177/0003702817736516, 2018.

Cook, N., Ciobanu, C. L., George, L., Zhu, Z.-Y., Wade, B., and Ehrig, K.: Trace Element Analysis of Minerals in Magmatic-Hydrothermal Ores by Laser Ablation Inductively-Coupled Plasma Mass Spectrometry: Approaches and Opportunities, Minerals, 6, 111, https://doi.org/10.3390/min6040111, 2016.

del Real, I., Thompson, J. F. H., Simon, A. C., and Reich, M.: Geochemical and Isotopic Signature of Pyrite as a Proxy for Fluid Source and Evolution in the Candelaria-Punta del Cobre Iron Oxide Copper-Gold District, Chile, Econ. Geol., 115, 1493–1518, https://doi.org/10.5382/econgeo.4765, 2020.

Elliott, N.: Interatomic Distances in FeS_2, CoS_2, and NiS_2, J. Chem. Phys., 33, 903–905, 1960.

Feng, J., Tian, H., Huang, Y., Ding, Z., and Yin, Z.: Directional Oxidation of Pyrite in Acid Solution, Minerals, 9, 7, https://doi.org/10.3390/min9010007, 2019.

Ferrer, I. J., Nevskaia, D. M., de las Heras, C., and Sánchez, C.: About the band gap nature of FeS_2 as determined from optical and photoelectrochemical measurements, Solid State Commun., 74, 913–916, https://doi.org/10.1016/0038-1098(90)90455-K, 1990.

Foucher, F., Guimbretière, G., Bost, N., and Westall, F.: Petrographical and Mineralogical Applications of Raman Mapping, in: Raman Spectroscopy and Applications, edited by: Maaz, K., InTechOpen publishing, 163–180, https://doi.org/10.5772/65112, 2017.

Fujioka, Y., Frantti, J., Puretzky, A., and King, G.: Raman Study of the Structural Distortion in the $Ni_{1-x}Co_xTiO_3$ Solid Solution, Inorg. Chem., 55, 9436–9444, https://doi.org/10.1021/acs.inorgchem.6b01693, 2016.

Goodwin, R., Corben, R., and Holland, L.: NI 43-101 Technical Report for the Punitaqui Project located near Ovalle, Chile, JDS Energy & Mining Inc., Vancouver, 2018.

Grant, H. L. J., Hannington, M. D., Petersen, S., Frische, M., and Fuchs, S. H.: Constraints on the behavior of trace elements in the actively-forming TAG deposit, Mid-Atlantic Ridge, based on LA-ICP-MS analyses of pyrite, Chem. Geol., 498, 45–71, https://doi.org/10.1016/j.chemgeo.2018.08.019, 2018.

Hope, G. A., Woods, R., and Munce, C. G.: Raman microprobe mineral identification, Miner. Eng., 14, 1565–1577, https://doi.org/10.1016/S0892-6875(01)00175-3, 2001.

Kinner, T., Bhandari, K. P., Bastola, E., Monahan, B. M., Haugen, N. O., Roland, P. J., Bigioni, T. P., and Ellingson, R. J.: Majority Carrier Type Control of Cobalt Iron Sulfide ($Co_xFe_{1-x}S_2$) Pyrite Nanocrystals, J. Phys. Chem. C, 120, 5706–5713, https://doi.org/10.1021/acs.jpcc.5b11204, 2016.

Klemm, D. D.: Synthesen und Analysen in den Dreiecksdiagrammen FeAsS–CoAsS–NiAsS und FeS_2–CoS_2–NiS_2, Neues Jb. Miner. Abh., 103, 205–255, https://doi.org/10.1127/njma/103/1965/205, 1965.

Kleppe, A. K. and Jephcoat, A. P.: High-pressure Raman spectroscopic studies of FeS_2 pyrite, Mineral. Mag., 68, 433–441, https://doi.org/10.1180/0026461046830196, 2004.

Kodera, P., Murphy, P. J., and Rankin, A. H.: Retrograde mineral reactions in saline fluid inclusions: The transformation ferropyrosmalite ? clinopyroxene, Am. Mineral., 88, 151–158, https://doi.org/10.2138/am-2003-0118, 2003.

Kwon, S. K., Youn, S. J., and Min, B. I.: Itinerant ferromagnetism in half-metallic CoS_2, Phys. Rev. B, 62, 357–360, https://doi.org/10.1103/PhysRevB.62.357, 2000.

Libowitzky, E.: Anisotropic pyrite: A polishing effect, Phys. Chem. Miner., 21, 97–103, https://doi.org/10.1007/BF00205220, 1994.

Lutz, H. D. and Willich, P.: Gitterschwingungsspektren. IX. Pyritstruktur. FIR-Spektren und Normalkoordinatenanalyse von MnS_2, FeS_2 und NiS_2, Z. Anorg. Allg. Chem., 405, 176–182, 1974.

Lutz, H. D. and Zwinscher, J.: Lattice dynamics of pyrite FeS_2 polarizable-ion model, Phys. Chem. Miner., 23, 497–502, https://doi.org/10.1007/bf00241999, 1996.

Macfarlane, R. M., Ushioda, S., and Blazey, K. W.: Resonant Raman scattering from FeS_2 (pyrite), Solid State Commun., 14, 851–855, 1974.

Mernagh, T. P. and Liu, L.-G.: Raman spectra from the Al_2SiO_5 polymorphs at high pressures and room temperature, Phys. Chem. Miner., 18, 126–130, 1991.

Mernagh, T. P. and Trudu, A. G.: A laser Raman microprobe study of some geologically important sulphide minerals, Chem. Geol., 103, 113–127, https://doi.org/10.1016/0009-2541(93)90295-T, 1993.

Nasdala, L., Smith, D. C., Kaindl, R., and Ziemann, M. A.: Raman spectroscopy: Analytical perspectives in mineralogical research, in: Spectroscopic methods in mineralogy, edited by: Beran, A. and Libowitzky, E., Mineralogical Society of Great Britain and Ireland, https://doi.org/10.1180/EMU-notes.6.7, 2004.

Osadchii, E. and Gorbaty, Y.: Raman spectra and unit cell parameters of sphalerite solid solutions ($Fe_xZn_{1-x}S$), Geochim. Cosmochim. Ac., 74, 568–573, https://doi.org/10.1016/j.gca.2009.10.022, 2010.

Pacˇevski, A., Libowitzky, E., Zˇivkovic´, P. A., Dimitrijevic´, R., and Cvetkovic´, L.: Copper-bearing pyrite from the Coka Marin polymetallic deposit, Serbia: Mineral inclusions or true solid solution?, Can. Mineral., 46, 249–261, https://doi.org/10.3749/canmin.46.1.249, 2008.

Pratt, J. L. and Bayliss, P.: Crystal-structure refinement of cattierite, Z. Krist.-Cryst. Mater., 150, 163–168, https://doi.org/10.1524/zkri.1979.150.14.163, 1979.

Sillitoe, R. H. and Thompson, J. F. H.: Intrusion–Related Vein Gold Deposits: Types, Tectono-Magmatic Settings and Difficulties of Distinction from Orogenic Gold Deposits, Resour. Geol., 48, 237–250, https://doi.org/10.1111/j.1751-3928.1998.tb00021.x, 1998.

Sourisseau, C., Cavagnat, R., and Fouassier, M.: The vibrational properties and valence force fields of FeS_2, RuS_2 pyrites and FeS_2 marcasite, J. Phys. Chem. Solids, 52, 537–544, https://doi.org/10.1016/0022-3697(91)90188-6, 1991.

Ushioda, S.: Raman scattering from phonons in iron pyrite (FeS_2), Solid State Commun., 10, 307–310, https://doi.org/10.1016/0038-1098(72)90013-0, 1972.

Vogt, H., Chattopadhyay, T., and Stolz, H. J.: Complete first-order Raman spectra of the pyrite structure compounds FeS_2, MnS_2 AND SiP_2, J. Phys. Chem. Solids, 44, 869–873, https://doi.org/10.1016/0022-3697(83)90124-5, 1983.

White, S. N.: Laser Raman spectroscopy as a technique for identification of seafloor hydrothermal and cold seep minerals, Chem. Geol., 259, 240–252, https://doi.org/10.1016/j.chemgeo.2008.11.008, 2008.

Xian, Y.-J., Wen, S.-M., Chen, X.-M., Deng, J.-S., and Liu, J.: Effect of lattice defects on the electronic structures and floatability of pyrites, Int. J. Min. Met. Mater., 19, 1069, https://doi.org/10.1007/s12613-012-0672-5, 2012.

Yuan, X. and Zheng, H.: In situ Raman spectroscopic studies of FeS_2 pyrite up to 675 K and 2100 MPa using a hydrothermal diamond anvil cell, Mineral. Mag., 79, 1–10, https://doi.org/10.1180/minmag.2015.079.1.01, 2015.

Zhou, L., McKenna, C. A., Long, D. G. F., and Kamber, B. S.: LA-ICP-MS elemental mapping of pyrite: An application to the Palaeoproterozoic atmosphere, Precambrian Res., 297, 33–55, https://doi.org/10.1016/j.precamres.2017.05.008, 2017.

Zhu, Q., Cook, N. J., Xie, G., Wade, B. P., and Ciobanu, C. L.: Arsenic-induced downshift of Raman band positions for pyrite, Econ. Geol., 115, 1589–1600, https://doi.org/10.5382/econgeo.4770, 2020.